

# The first-principles phase diagram of monolayer nanoconfined water

<https://doi.org/10.1038/s41586-022-05036-x>

Received: 22 October 2021

Accepted: 28 June 2022

Published online: 14 September 2022

 Check for updates

Venkat Kapil<sup>1</sup>✉, Christoph Schran<sup>1,2,3</sup>✉, Andrea Zen<sup>4,5</sup>, Ji Chen<sup>6</sup>, Chris J. Pickard<sup>7,8</sup> & Angelos Michaelides<sup>1,2,3</sup>✉

Water in nanoscale cavities is ubiquitous and of central importance to everyday phenomena in geology and biology. However, the properties of nanoscale water can be substantially different from those of bulk water, as shown, for example, by the anomalously low dielectric constant of water in nanochannels<sup>1</sup>, near frictionless water flow<sup>2</sup> or the possible existence of a square ice phase<sup>3</sup>. Such properties suggest that nanoconfined water could be engineered for technological applications in nanofluidics<sup>4</sup>, electrolyte materials<sup>5</sup> and water desalination<sup>6</sup>. Unfortunately, challenges in experimentally characterizing water at the nanoscale and the high cost of first-principles simulations have prevented the molecular-level understanding required to control the behaviour of water. Here we combine a range of computational approaches to enable a first-principles-level investigation of a single layer of water within a graphene-like channel. We find that monolayer water exhibits surprisingly rich and diverse phase behaviour that is highly sensitive to temperature and the van der Waals pressure acting within the nanochannel. In addition to multiple molecular phases with melting temperatures varying non-monotonically by more than 400 kelvins with pressure, we predict a hexatic phase, which is an intermediate between a solid and a liquid, and a superionic phase with a high electrical conductivity exceeding that of battery materials. Notably, this suggests that nanoconfinement could be a promising route towards superionic behaviour under easily accessible conditions.

In the past decades, approaches have been devised to fabricate artificial hydrophobic capillaries with nanoscale dimensions<sup>7–9</sup>, resulting in measurements of the properties of nanoconfined water<sup>1–3</sup>. Despite these notable advances, the understanding of nanoconfined water is still limited, owing to the difficulty in interpreting these experiments in the absence of simultaneous information on the atomistic-scale structure and dynamics of water that is not yet accessible in these experiments. Molecular simulations can, in principle, provide the required resolution but the results obtained are highly sensitive to the approach used, even for a single layer of water within graphene confinement. For example, studies involving inexpensive empirical water models have predicted varied phase behaviour depending on the choice of the model<sup>10,11</sup>. Furthermore, their non-reactive nature makes them unsuitable for studying water at high pressures at which water can dissociate and even exhibit superionic behaviour<sup>12,13</sup>. By contrast, more accurate first-principles studies of nanoconfined water, using density functional theory (DFT), are limited by their large computational cost and have therefore been limited to only 0 K calculations, or a handful of finite-temperature state points<sup>14</sup>. Thus, the absence of accurate but affordable first-principles approaches that can be used to examine a range of temperatures and pressures has led to a general lack of

knowledge on the phase behaviour of nanoconfined water, ranging from different stable phases, melting temperatures and the nature of phase transitions, to the physical properties relevant to nanotechnology. A clear understanding of the phases and properties of confined water as a function of thermodynamic parameters will facilitate the interpretation of experiments, and provide a foundation for the rational design of improved nanotechnologies.

Here we describe the phase behaviour of monolayer-confined water by calculating its pressure–temperature phase diagram at first-principles accuracy. We avoid the traditional accuracy–cost trade-off by using quantum Monte Carlo (QMC), one of the most accurate first-principles methods for molecular materials<sup>15</sup>, to identify the most appropriate DFT functional for the systems under investigation. We subsequently developed a machine learning potential (MLP) using the approach recently introduced in ref.<sup>16</sup> to predict DFT energies and forces at a much lower cost. This framework brings together the high accuracy of QMC and the low computational cost of MLPs, enabling us to examine the pressure–temperature phase diagram, including the dissociation regime. In doing so, we reconcile inconsistencies between previous studies, identify phases and properties of confined water that can be harnessed for nanotechnology, and provide guidance for future experimental exploration.

<sup>1</sup>Yusuf Hamied Department of Chemistry, University of Cambridge, Cambridge, UK. <sup>2</sup>Department of Physics and Astronomy, University College London, London, UK. <sup>3</sup>Thomas Young Centre, London Centre for Nanotechnology, London, UK. <sup>4</sup>Dipartimento di Fisica Ettore Pancini, Università di Napoli Federico II, Napoli, Italy. <sup>5</sup>Department of Earth Sciences, University College London, London, UK. <sup>6</sup>School of Physics, Interdisciplinary Institute of Light-Element Quantum Materials and Frontiers Science Center for Nano-optoelectronics, Peking University, Beijing, China.

<sup>7</sup>Department of Materials Science and Metallurgy, University of Cambridge, Cambridge, UK. <sup>8</sup>Advanced Institute for Materials Research, Tohoku University, Sendai, Japan.

✉e-mail: vk380@cam.ac.uk; cs2121@cam.ac.uk; am452@cam.ac.uk

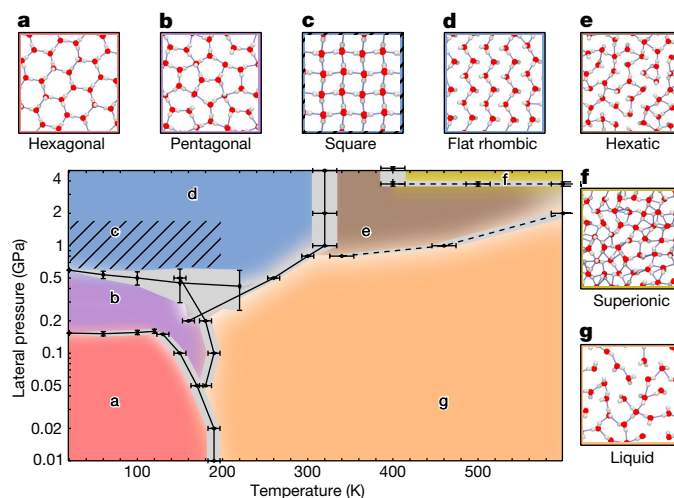


**Fig. 1 | Phase diagram of monolayer nanoconfined water.** **a–g**, The pressure–temperature phase diagram of monolayer water was calculated using an MLP that delivers first-principles accuracy. The solid and dashed lines indicate first-order and continuous phase transitions, respectively. The grey regions indicate the statistical uncertainty for solid–solid phase transitions and, for the other transitions, the uncertainties arising from studying a finite number of

thermodynamic states. The diagonally hatched area indicates the region in which square and flat-rhombic phases are near degenerate. Diagrams of the hexagonal (**a**), pentagonal (**b**), square (**c**), flat-rhombic (**d**), hexatic (**e**), superionic (**f**) and liquid (**g**) phases are shown with oxygen atoms in red, hydrogen atoms in grey and hydrogen bonds shown by blue lines.

## Extensive polymorph search using an MLP

Water under nanoconfinement experiences a lateral pressure due to a combination of attractive van der Waals forces pulling the sheets of the confining material and the termination of the cavities. The exact value of this lateral pressure within graphene confinement is not known, but computational studies and experiments suggest that it is in the range of 0.5–1.5 GPa (ref. <sup>3</sup>). These pressures can stabilize polymorphs of ice that are not found in bulk<sup>17,18</sup>. However, the lateral pressure depends on the magnitude of the van der Waals forces<sup>19</sup> as well as on the shape and mechanical response of the terminal edges of the cavity<sup>20</sup>, both of which are sensitive to the nature of the confining material. Thus, studying the phase behaviour of nanoconfined water across a broad range of pressures, beyond the expected 0.5–1.5 GPa regime, is relevant for a general understanding of the properties of water in hydrophobic nanocavities.

Before computing the phase diagram, we identified all polymorphs stabilized by lateral pressures between 0 and 4 GPa. To accurately account for the full range of interactions in nanoconfined water, while ensuring a viable computational cost to perform an extensive structure search, we used an MLP trained on first-principles energies and forces. We used QMC benchmarks to select the revPBE0-D3 DFT functional for treating water–water interactions in confinement (a comparison is shown in Extended Data Table 1), and subsequently trained and validated an MLP to revPBE0-D3 across the entire phase diagram, using an advanced active-learning approach<sup>16</sup> (details on the training and validation are shown in Extended Data Fig. 1). We treated graphene–water interactions using a uniform 2D confining potential fitted to QMC water–graphene binding energies and applied an external lateral pressure<sup>10,11,17,21</sup> to model the internal lateral pressure on the water molecules.

Owing to the computational efficiency of the MLP, we can perform an exhaustive structure search<sup>22</sup>. We recovered all previously found polymorphs<sup>17,18</sup> in only a few hours on a desktop machine, and found a ‘flat rhombic’ phase at high pressures (Extended Data Fig. 2). This structure is stabilized by a strong network of zig-zagging hydrogen bonds, differing from the motifs present in flat-rhombic phases observed in empirical force-field studies<sup>10,11</sup>. We attribute the differences to the rigid water models used in these studies that do not describe the complex

hydrogen bond network arising from the full spectrum of O–H distances and H–O–H angles present in our structures (Extended Data Fig. 2). To establish the relative stability of this new phase, we used enthalpies calculated with QMC at 0 and 2 GPa (Extended Data Table 1). In agreement with previous results, hexagonal ice has the lowest enthalpy at 0 GPa (ref. <sup>21</sup>); however, beyond 2 GPa, we found that the flat-rhombic phase becomes the dominant form, being more stable than square ice by about 1 kJ mol<sup>-1</sup> (Extended Data Fig. 3).

Encouraged by the success of the MLP in exhaustively identifying monolayer polymorphs, and to find the MLP predictions within 1 kJ mol<sup>-1</sup> of the QMC references (Extended Data Table 1), we proceeded to examine the pressure–temperature phase diagram. We selected a small confinement width of 5 Å, as the effects of nanoconfinement should be the largest in the narrow width regime. As described in the Methods, we used a range of rigorous free-energy methods to calculate the phase boundaries<sup>23</sup>. The resulting phase diagram (Fig. 1) is extremely complex and diverse for a deceptively simple monolayer of water. The phase behaviour is very sensitive to the lateral pressure and, therefore, we discuss below the phase diagram in different pressure regimes: low pressures below 0.5 GPa; intermediate pressures from 0.5–2.0 GPa, that is, at the expected lateral van der Waals pressure within graphene confinement; and high pressures above 2.0 GPa. As seen from Extended Data Tables 2 and 3 and Extended Data Fig. 4, our predictions are robust with respect to the choice of the confining potential, small (–0.5 Å) changes in the confinement width, as well as finite-size effects. We also show that nuclear quantum effects have only a small effect on the phase boundaries; for clarity, these were therefore not taken into account in Fig. 1.

## Rich phase behaviour at low pressures

Like bulk water, hexagonal ice is the most stable phase at zero pressure for monolayer water. As the pressure is increased, pentagonal and flat-rhombic forms become the most stable phases at around 0.15 GPa and 0.5 GPa, respectively. Our QMC calculations show that the flat-rhombic phase is the most stable phase at high pressures; however, at intermediate pressures, it is only marginally more stable (within the statistical error of QMC) than the square phase. Thus, we have marked

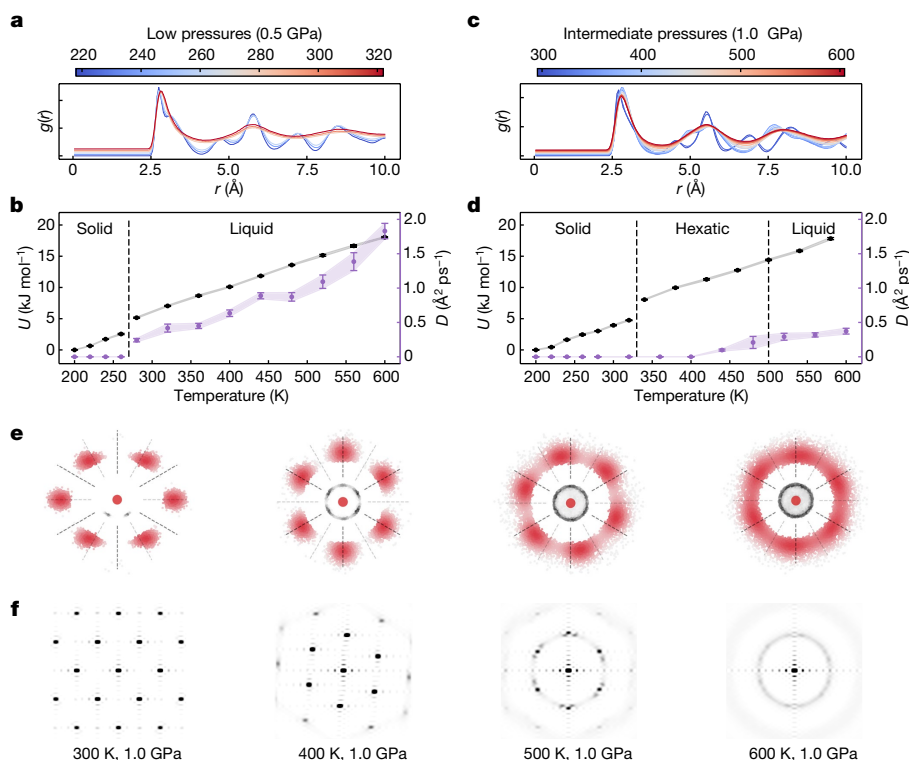


**Fig. 2 | Hexatic phase of monolayer water at intermediate pressures.**

**a,b,** The lateral distribution function of oxygen atoms  $g(r)$  at different temperatures (**a**) and the potential energy  $U$  (black) and the diffusion coefficient  $D$  (violet) (**b**) as a function of temperature at 0.5 GPa, indicating a first-order phase transition. **c,d,** The lateral distribution function of oxygen atoms  $g(r)$  at different temperatures (**c**) and the potential energy (black) and the diffusion coefficient (violet) (**d**) as a function of temperature at 1.0 GPa, indicating a first-order phase transition to a hexatic phase, and a continuous phase transition to the liquid phase. **e,** The temperature-dependent spatial

distribution of the oxygen atoms in the first hydration shell (red) and the bonded hydrogen (black) atoms with respect to an oxygen atom at 300–600 K at 1 GPa. The darker colours indicate higher spatial probabilities, and radial rulers are guides for examining six-fold orientational symmetry—characteristic of a hexatic phase. **f,** Temperature-dependent structure factors, indicating the loss of translational order in the hexatic phase at 400 K, and the loss of orientational order in the liquid at 600 K, at 1.0 GPa. Error bars correspond to s.e.m. calculated using block averaging.

a narrow region on our phase diagram in which the square phase could compete in thermodynamic stability with the flat-rhombic phase.

To understand the melting behaviour of monolayer ice, we calculated the coexistence lines of the solid and the liquid phases. We found that hexagonal ice exhibits a low melting temperature of around 190 K at 0 GPa, about 100 K lower than that of bulk water, and 50–100 K lower than the estimates from empirical force fields<sup>10,24</sup>. As shown in Fig. 1, we observed a triple point at around 170 K and 0.05 GPa between the hexagonal, pentagonal and liquid phases (Supplementary Video 1). As the pressure was increased, we observed a second triple point between the flat-rhombic, pentagonal and liquid phases (Supplementary Video 2) at around 160 K and 0.20 GPa. We also note that the hexagonal, pentagonal and flat-rhombic phases can be denser or rarer than the liquid phase, which leads to a non-monotonic dependence of the melting temperature with pressure. This suggests that monolayer water may expand or contract after melting, depending on the pressure. Thus, overall, we found that, at pressures of less than 0.5 GPa, monolayer ice exhibits complex polymorphism, two triple points and a non-monotonic melting temperature with pressure. These insights are expected to be key for the thermal or mechanical engineering of water-based nanodevices.

### Hexatic phase at intermediate pressures

In the intermediate pressure regime, that is, at typical van der Waals pressures between 0.5 and 2.0 GPa in graphene confinement, monolayer water exhibits a phase that is neither solid nor liquid. As shown in Fig. 2a,b, below 0.8 GPa, flat-rhombic ice melts through a first-order

phase transition accompanied by abrupt changes in the enthalpy and the structure of water, as well as in the diffusion coefficient. However, beyond this pressure, flat-rhombic ice undergoes a first-order phase transition to a new phase with rotating water molecules. As evidenced in the structure-factor (Fig. 2f), the new phase lacks translational order but exhibits six-fold orientational symmetry. Furthermore, the angular nodes in the spatial distributions of oxygen atoms (Fig. 2e) indicate long-range orientational order. These properties suggest that the phase bears hallmarks of a hexatic phase, an intermediate phase between the solid and the liquid within the theory of phase transitions in 2D<sup>25</sup> by Kosterlitz, Thouless, Halperin, Nelson and Young (KTHNY) theory.

The hexatic phase, at 340 K, is characterized by fixed but rotating water molecules as visualized from the 2D spatial distribution of hydrogen atoms (Supplementary Video 3), bearing similarities with the high-pressure free-rotor phase of molecular hydrogen<sup>26</sup>. A close look at the rotational dynamics (Supplementary Video 3) and the spatial distribution of atoms (Fig. 2e) suggests that the pseudorotation comprises out-of-plane motion of O–H bonds through intermediate dangling orientations, with less-frequent in-plane rotations. With an increase in temperature, the in-plane rotation becomes facile, resulting in the loss of six-fold orientational symmetry and the formation of an isotropic liquid as shown in Fig. 2e. The hexatic phase melts with smooth changes in enthalpy, structure and diffusion coefficient, indicating a second-order phase transition in agreement with the KTHNY theory. In short, at typical pressures experienced in graphene confinement, the melting behaviour of monolayer water deviates substantially from that of bulk water, exhibiting a two-step

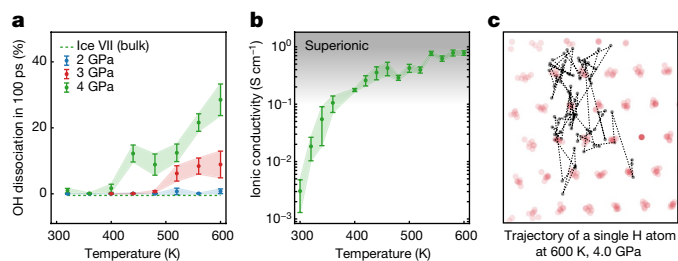


**Fig. 3 | Superionic behaviour at high pressures.** **a**, Temperature dependence of the percentage of dissociated OH bonds in monolayer (circles) and bulk (dashed line) water in 100 ps, at 2 GPa (blue), 3 GPa (red) and 4 GPa (green). The values for ice VII at 4 GPa are all almost zero but have been vertically adjusted to a small negative value for clarity. **b**, Temperature-dependent ionic conductivity of monolayer water at 4 GPa. The grey region indicates the advent of the superionic regime. **c**, The spatial distribution of oxygen atoms (red) with respect to an arbitrarily chosen oxygen atom, and the trajectory of a single hydrogen atom (black) at 600 K and 4 GPa, indicating facile proton transfer. Error bars correspond to s.e.m. calculated using block averaging.

mechanism, in agreement with KTHNY theory, through a hexatic phase with ‘rotating’ water molecules.

Although the hallmarks of an intermediate hexatic phase have been discussed qualitatively in previous forcefield studies<sup>27</sup>, our first-principles-level prediction in the intermediate pressure regime suggests that this phase can be realized experimentally in graphene confinement. We provide further support for this by simulating water between explicit graphene sheets at the reference first-principles level (Supplementary Video 6), and observing hexatic behaviour in agreement with the prediction of our MLP. Finally, to facilitate the identification of this phase, we calculated the rotational relaxation time of water molecules and the temperature-dependent vibrational spectra, which can be compared using nuclear magnetic resonance and Raman spectroscopy measurements, respectively (Extended Data Fig. 5).

### Superionic behaviour at high pressures

One of the key features of our water model is its ability to describe water dissociation, which becomes increasingly relevant at high pressures. We therefore examined the possibility of autoprotolysis events in monolayer water. We found that, at pressures beyond 2 GPa and temperatures beyond 350 K, O–H bond breaking and formation events frequently occur. To quantify O–H dissociation, we analysed the average number of dissociated water molecules within 100 ps at different pressures and temperatures. As shown in Fig. 3a, at 4 GPa and beyond 400 K, over 10% of the water molecules dissociate in monolayer water within 100 ps. By contrast, this percentage remains close to zero for the corresponding bulk phase (ice VII) even at the highest temperature considered. We attribute this substantially greater propensity for dissociation to an approximate 10% decrease in O–O distances in monolayer water compared to the bulk water; it is known that the O–O distance modulates the proton transfer barrier<sup>28</sup>. We also note that oxygen atoms remain localized, but protons readily diffuse through the oxygen lattice (Fig. 3c and Supplementary Video 4). This behaviour is characteristic of the recently observed superionic phase of water<sup>13</sup>, which is believed to be found under extreme planetary conditions. To ascertain whether we are in the superionic regime, we estimated the ionic conductivity of monolayer water as a function of temperature at 4 GPa. As shown in Fig. 3b, water ‘continuously’ transforms to a phase with a specific ionic conductance above  $0.1 \text{ S cm}^{-1}$ , a commonly used threshold for characterizing a superionic conductor<sup>29</sup>. This is intriguing as bulk water exhibits superionic behaviour at 56 GPa and over 700 K (ref. 30), which is an order of magnitude greater pressure and almost twice the temperature compared with for monolayer water.

To clarify whether our observations correspond to a conventional superionic phase of water in which protons diffuse within a matrix of oxygen atoms or a phase in which ionic conductivity occurs through surface hopping of protons, we performed first-principles simulations with explicit graphene sheets (Supplementary Video 5). Although within explicit graphene sheets have the opportunity to stick to and hydrogenate the graphene sheet, these simulations confirm the results obtained with the MLP: there is facile O–H dissociation and long-range proton diffusion without the formation of C–H bonds. This observation is consistent with the known affinities of protons with carbon and oxygen and, importantly, it suggests that nanoconfined water can exhibit genuine superionic behaviour as opposed to an interfacial layer with high ionic conductivity.

The enhanced propensity of autoprotolysis in confined water should be manifested at typical lateral pressures in the in-plane component of the dielectric constant that is sensitive to excursions of protons along the O–H bonds. This property can already be measured for nanoconfinement between graphene and other hydrophobic materials<sup>1</sup>. Direct observation of superionic conduction may require lateral pressures higher than those typically exerted by graphene sheets. To this extent, it may be useful to understand how the lateral pressures can be tuned by altering the morphology of different confining materials. Experiments already suggest that graphene sheets distorted through ‘nanobubbles’ can exert pressures in the tens of GPa regime<sup>20</sup> over a length scale of tens of nanometres. We believe that nanocavities made of similarly deformed materials could be a starting point towards high-pressure confinement.

### Conclusions

We predict the pressure–temperature phase diagram of monolayer-confined water rigorously at first-principles accuracy—from low temperatures and pressures up to the dissociation regime of water. A comprehensive description of the complex behaviour of nanoconfined water across the temperature–pressure phase diagram provides new insights, a guide for future experiments and a starting point for rational material design in the context of nanotechnology. The existence of a two-step melting mechanism in agreement with KTHNY theory and a hexatic phase provides new physical insights that the melting of water at the nanoscale may not necessarily be first-ordered as in bulk, and may have direct implications in the thermal engineering of nanosystems. The evidence for increased water dissociation in nanoconfinement provides a basis for rationalizing anomalous properties of nanoconfined water, for example, the low slippage in water flow in h-BN<sup>2</sup> could be understood on the basis of the enhanced propensity of O–H dissociation in nanoconfined water. Furthermore, the large electrical conductivity of superionic nanoconfined water could be harnessed for the development of aqueous electrolytes. Finally, our research suggests that nanoconfinement could be a route towards examining superionic materials under easily accessible conditions.

### Online content

Any methods, additional references, Nature Research reporting summaries, source data, extended data, supplementary information, acknowledgements, peer review information; details of author contributions and competing interests; and statements of data and code availability are available at <https://doi.org/10.1038/s41586-022-05036-x>.

1. Fumagalli, L. et al. Anomalously low dielectric constant of confined water. *Science* **360**, 1339–1342 (2018).
2. Secchi, E. et al. Massive radius-dependent flow slippage in carbon nanotubes. *Nature* **537**, 210–213 (2016).
3. Algara-Siller, G. et al. Square ice in graphene nanocapillaries. *Nature* **519**, 443–445 (2015).
4. Kavokine, N., Bocquet, M.-L. & Bocquet, L. Fluctuation-induced quantum friction in nanoscale water flows. *Nature* **602**, 84–90 (2022).
5. Hummer, G., Rasaiah, J. C. & Noworyta, J. P. Water conduction through the hydrophobic channel of a carbon nanotube. *Nature* **414**, 188–190 (2001).

6. Surwade, S. P. et al. Water desalination using nanoporous single-layer graphene. *Nat. Nanotechnol.* **10**, 459–464 (2015).
7. Radha, B. et al. Molecular transport through capillaries made with atomic-scale precision. *Nature* **538**, 222–225 (2016).
8. Geim, A. K. & Grigorieva, I. V. Van der Waals heterostructures. *Nature* **499**, 419–425 (2013).
9. Niguès, A., Siria, A., Vincent, P., Poncharal, P. & Bocquet, L. Ultrahigh interlayer friction in multiwalled boron nitride nanotubes. *Nat. Mater.* **13**, 688–693 (2014).
10. Zhu, Y., Wang, F. & Wu, H. Superheating of monolayer ice in graphene nanocapillaries. *J. Chem. Phys.* **146**, 134703 (2017).
11. Li, S. & Schmidt, B. Replica exchange MD simulations of two-dimensional water in graphene nanocapillaries: rhombic versus square structures, proton ordering, and phase transitions. *Phys. Chem. Chem. Phys.* **21**, 17640–17654 (2019).
12. Millot, M. et al. Nanosecond X-ray diffraction of shock-compressed superionic water ice. *Nature* **569**, 251–255 (2019).
13. Millot, M. et al. Experimental evidence for superionic water ice using shock compression. *Nat. Phys.* **14**, 297–302 (2018).
14. Jiang, J. et al. First-principles molecular dynamics simulations of the spontaneous freezing transition of 2D water in a nanoslit. *J. Am. Chem. Soc.* **143**, 8177–8183 (2021).
15. Zen, A. et al. Fast and accurate quantum Monte Carlo for molecular crystals. *Proc. Natl Acad. Sci. USA* **115**, 1724–1729 (2018).
16. Schran, C. et al. Machine learning potentials for complex aqueous systems made simple. *Proc. Natl Acad. Sci. USA* **118**, e2110077118 (2021).
17. Corsetti, F., Matthews, P. & Artacho, E. Structural and configurational properties of nanoconfined monolayer ice from first principles. *Sci. Rep.* **6**, 18651 (2016).
18. Chen, J., Schusteritsch, G., Pickard, C. J., Salzmann, C. G. & Michaelides, A. Two dimensional ice from first principles: structures and phase transitions. *Phys. Rev. Lett.* **116**, 025501 (2016).
19. Björkman, T., Gulans, A., Krasheninnikov, A. V. & Nieminen, R. M. van der Waals bonding in layered compounds from advanced density-functional first-principles calculations. *Phys. Rev. Lett.* **108**, 235502 (2012).
20. Zamborlini, G. et al. Nanobubbles at GPa pressure under graphene. *Nano Lett.* **15**, 6162–6169 (2015).
21. Chen, J., Zen, A., Brandenburg, J. G., Alfé, D. & Michaelides, A. Evidence for stable square ice from quantum Monte Carlo. *Phys. Rev. B* **94**, 220102 (2016).
22. Pickard, C. J. & Needs, R. J. Ab initio random structure searching. *J. Phys. Condens. Matter* **23**, 053201 (2011).
23. Kapil, V. & Engel, E. A. A complete description of thermodynamic stabilities of molecular crystals. *Proc. Natl Acad. Sci. USA* **119**, e2111769119 (2022).
24. Ferguson, A. L., Giovambattista, N., Rossky, P. J., Panagiotopoulos, A. Z. & Debenedetti, P. G. A computational investigation of the phase behavior and capillary sublimation of water confined between nanoscale hydrophobic plates. *J. Chem. Phys.* **137**, 144501 (2012).
25. Kosterlitz, J. M. & Thouless, D. J. Ordering, metastability and phase transitions in two-dimensional systems. *J. Phys. C Solid State Phys.* **6**, 1181–1203 (1973).
26. Pickard, C. J. & Needs, R. J. Structure of phase III of solid hydrogen. *Nat. Phys.* **3**, 473–476 (2007).
27. Vilanova, O. & Franzese, G. Structural and dynamical properties of nanoconfined supercooled water. Preprint at *arXiv* <http://arxiv.org/abs/1102.2864> (2011).
28. Muñoz-Santiburcio, D. & Marx, D. Confinement-controlled aqueous chemistry within nanometric slit pores. *Chem. Rev.* **121**, 6293–6320 (2021).
29. Kreuer, K.-D. Proton conductivity: materials and applications. *Chem. Mater.* **8**, 610–641 (1996).
30. Sugimura, E. et al. Experimental evidence of superionic conduction in H<sub>2</sub>O ice. *J. Chem. Phys.* **137**, 194505 (2012).

**Publisher's note** Springer Nature remains neutral with regard to jurisdictional claims in published maps and institutional affiliations.

Springer Nature or its licensor holds exclusive rights to this article under a publishing agreement with the author(s) or other rightsholder(s); author self-archiving of the accepted manuscript version of this article is solely governed by the terms of such publishing agreement and applicable law.

© The Author(s), under exclusive licence to Springer Nature Limited 2022

## Methods

To ensure that our approach remained both computationally efficient and accurate, we used a combination of these four developments: (1) an efficient implementation of QMC to select a DFT functional; (2) an automated development and validation of the MLP to DFT energies and forces; (3) random structure search with the MLP to find metastable polymorphs; and (4) rigorous Gibbs free energies as the basis for thermodynamic stabilities of polymorphs. Step 1 attenuates the limitations of DFT by identifying the most appropriate DFT functional for the system under study, and makes accurate first-principles energies and forces accessible for training an MLP, at a much lower cost than high-level electronic structure methods. Step 2 substantially reduces the human time required to develop an MLP trained on DFT energies and forces. Step 3 ensures an exhaustive search (owing to the low cost of the MLP) for metastable polymorphs of the system. Step 4 enables the realistic modelling of experimental thermodynamic conditions and calculation of observables that can be directly compared with experiments.

Below, we discuss the full workflow for the calculation of the phase diagram and the computational details.

### Workflow

**Separation of the potential energy surface.** We split the total potential energy of the system into graphene–water interactions modelled using a uniform 2D confining potential fitted to QMC water–graphene binding energies<sup>18</sup>, and water–water interactions at the DFT level of theory. The confining potential acts only in the direction perpendicular to the plane of confinement, as in previous studies<sup>11,21</sup>. We model the lateral pressure,  $P_{xy}$ , due to the van der Waals interactions pulling the graphene sheets and the termination of the edges, by applying an external lateral pressure within the  $NP_{xy}T$  ensemble, where  $N$  is the number of atoms in the system and  $T$  is the temperature.

**Selection of an accurate DFT level for water–water interactions.** We exploit the chemical accuracy and efficiency of a recent fixed-node diffusion Monte Carlo implementation of QMC<sup>15</sup>, to provide lattice energies of a few known phases of monolayer water<sup>18</sup>—hexagonal, pentagonal, square and buckled-rhombic ice. These values are used as references to screen suitable DFT functionals for water–water interactions. From these validation tests, we select revPBE0-D3 as it exhibits one of the smallest errors in lattice energies, and is also known to provide a good description of the properties of bulk water<sup>31</sup>.

**Development of the MLP to DFT.** We trained an MLP to reproduce revPBE0-D3 energies and forces to probe new phases of monolayer confined water and their phase behaviour across a wide range of temperatures and pressures, in an accurate and efficient manner. To minimize the time spent in developing the potential, we use a recently proposed active learning scheme<sup>16</sup>. It relies on the Behler–Parrinello neural network framework<sup>32</sup> to form a committee neural network potential<sup>33</sup> for active learning purposes. With this workflow, we target various phase points in the course of different generations as detailed in Fig. 1. Our final potential exhibits a root mean square error of 2.4 meV (0.2 kJ mol<sup>-1</sup>) per water molecule and 75 meV Å<sup>-1</sup> for energies and forces, respectively. Furthermore, the MLP also reproduces the good agreement of revPBE0-D3 with QMC reference lattice energies as shown in Extended Data Table 1 and remains accurate over the entire phase diagram, while retaining excellent performance for condensed phase properties as shown in Fig. 1.

**Random structure search.** We probe potential phases of monolayer ice using the random structure search approach<sup>22</sup> in combination with the MLP. Within this approach, we optimize a large set of structures generated by randomly placing water molecules within the region of

confinement for unit cells with 2 to 72 water molecules, confinement widths ranging from 5 to 8 Å, and lateral pressures from 0 to 4 GPa. We recover all previously known ice polymorphs, and also find a new flat-rhombic phase that is stable at high pressures.

**Calculation of phase boundaries.** With the knowledge of stable and metastable phases, we calculate their regions of stabilities by computing their Gibbs free energies,  $G(P, T)$ , using a thermodynamic integration approach<sup>23</sup>. At each pressure, we calculate the classical harmonic Helmholtz free energy at 20 K ( $A_{20\text{K}}^{\text{harm}}$ ) of a given polymorph, and perform a harmonic-to-anharmonic thermodynamic integration to estimate

$$G(P, T_{20\text{K}}) = A_{20\text{K}}^{\text{harm}} + \Delta A_{20\text{K}}^{\text{anharm}} + PV + k_{\text{B}}(20\text{K}) \ln p(V)_{P,20\text{K}}, \quad (1)$$

where  $V$  is the volume of the structure optimized at pressure  $P$ ,  $p(V)_{P,20\text{K}}$  is its probability density of observing a volume  $V$  at 20 K and pressure  $P$ , and  $k_{\text{B}}$  is the Boltzmann constant. The temperature-dependent Gibbs free energy is estimated from a thermodynamic integration over temperature. The phase diagram for the polymorphs is calculated by identifying the phase with the lowest Gibbs free energy at each  $P, T$ .

The solid to disordered phase boundary at each pressure is calculated by monitoring migration of phase boundaries in direct coexistence simulations<sup>34</sup>. The initial configurations for these simulations are generated carefully in three steps: (1) we thermalize a  $2 \times 1 \times 1$  simulation cell of a polymorph at  $P, T$ ; (2) we fix the oxygen atoms of one half of the cell and melt the other half, and subsequently cool the full system to  $T$  in the (constrained) NVT ensemble; (3) relax the density of the full system in the  $NP_xT$  ensemble.

To estimate the boundary of the continuous phase transition between the hexatic-like and the liquid phase, we use a criterion based on six-fold orientational symmetry. Using these approaches in combination with MLPs, we take into account finite temperature thermodynamics at first-principles accuracy. We also check the importance quantum nuclear effects by performing a path-integral molecular dynamics simulation. In all cases we calculate uncertainties due to statistical and systematic errors.

### Computational details

All MLP simulations are performed using the i-PI<sup>35</sup> code with the n2p2-LAMMPS<sup>36</sup> library to calculate the MLP energies and forces, and an ASE<sup>37</sup> driver for the uniform confining potential. Simulation supercells containing 144 molecules are used for all phases after carefully examining finite size effects. Electrical conductivities are estimated using Green–Kubo theory on the basis of atomistic velocities and fixed atomistic oxidation numbers<sup>38</sup>. The revPBE0-D3 calculations are performed using CP2K<sup>39</sup> with computational settings from an earlier publication<sup>40</sup>.

The first-principles molecular dynamics simulations are carried out with the CP2K package using the revPBE-D3 and revPBE0-D3 functionals. The model consists of two layers of graphene and an embedded layer of 2D ice. The superionic and the hexatic structures were stretched slightly (<10%) to fit the lattice of graphene supercells. The supercell, including the vacuum slab, is  $12.3 \times 8.52144 \times 20.0$  Å. In each graphene layer, eight evenly distributed atoms were not allowed to move along the perpendicular direction during the AIMD simulations to avoid buckling. The hexatic and superionic phase were simulated at 400 K and 600 K in the NVT ensemble, for 50 ps at revPBE-D3 level and for 10 ps at revPBE0-D3 level. Both sets of simulations exhibited the same qualitative behaviour.

The QMC calculations are performed using the CASINO package<sup>41</sup> using Dirac–Fock pseudopotentials with the locality approximations<sup>42</sup>, while taking into account errors due to finite time step and systems sizes<sup>15</sup>.

More technical details of all the simulations/calculations are provided in their corresponding input files in the Source data.

## Data availability

The initial structures required to reproduce the key findings of this work are available at GitHub (<https://github.com/venkatkapil24/data-monolayer-confined-water-phase-diagram/>).

## Code availability

The scripts and codes to reproduce the key findings of this work are available at GitHub (<https://github.com/venkatkapil24/data-monolayer-confined-water-phase-diagram/>).

31. Cheng, B., Engel, E. A., Behler, J., Dellago, C. & Ceriotti, M. Ab initio thermodynamics of liquid and solid water. *Proc. Natl Acad. Sci.* **116**, 1110–1115 (2019).
32. Behler, J. Four generations of high-dimensional neural network potentials. *Chem. Rev.* <https://doi.org/10.1021/acs.chemrev.0c00868> (2021).
33. Schran, C., Brezina, K. & Marsalek, O. Committee neural network potentials control generalization errors and enable active learning. *J. Chem. Phys.* **153**, 104105 (2020).
34. Conde, M. M., Gonzalez, M. A., Abascal, J. L. F. & Vega, C. Determining the phase diagram of water from direct coexistence simulations: the phase diagram of the TIP4P/2005 model revisited. *J. Chem. Phys.* **139**, 154505 (2013).
35. Kapil, V. et al. Universal Force Engine For Advanced Molecular Simulations. *Comput. Phys. Commun.* **236**, 214–223 (2019).
36. Singraber, A., Behler, J. & Dellago, C. Library-based LAMMPS implementation of high-dimensional neural network potentials. *J. Chem. Theory Comput.* **15**, 1827–1840 (2019).
37. Larsen, A. H. et al. The atomic simulation environment—a Python library for working with atoms. *J. Phys. Condens. Matter* **29**, 273002 (2017).
38. Grasselli, F. & Baroni, S. Topological quantization and gauge invariance of charge transport in liquid insulators. *Nat. Phys.* **15**, 967–972 (2019).
39. Kühne, T. D. et al. CP2K: an electronic structure and molecular dynamics software package—Quickstep: efficient and accurate electronic structure calculations. *J. Chem. Phys.* **152**, 194103 (2020).
40. Marsalek, O. & Markland, T. E. Quantum dynamics and spectroscopy of ab initio liquid water: the interplay of nuclear and electronic quantum effects. *J. Phys. Chem. Lett.* **8**, 1545–1551 (2017).
41. Needs, R. J., Towler, M. D., Drummond, N. D. & Rios, P. L. Continuum variational and diffusion quantum Monte Carlo calculations. *J. Phys. Condens. Matter* **22**, 023201 (2010).
42. Mitas, L., Shirley, E. L. & Ceperley, D. M. Nonlocal pseudopotentials and diffusion Monte Carlo. *J. Chem. Phys.* **95**, 3467 (1991).
43. Brandenburg, J. G. et al. Physisorption of water on graphene: subchemical accuracy from many-body electronic structure methods. *J. Phys. Chem. Lett.* **10**, 358–368 (2019).

**Acknowledgements** We thank D. Frenkel for discussions; D. M. Wilkins for providing the code to study the angular orientation of water; F. L. Thiemann for help with hydrogen bond analysis; M. Davies for help with visualization and graphics; P. Ravindra for reading the manuscript; and the staff at the UK Materials and Molecular Modelling Hub for computational resources, which is partially funded by Engineering and Physical Sciences Research Council (grants EP/P020194/1 and EP/T022213/1). V.K. acknowledges funding from the Swiss National Science Foundation (SNSF) under project P2ELP2\_191678 and the Ernest Oppenheimer Fund, allocation of CPU hours by CSCS under Project ID s1000 and support from Churchill College, University of Cambridge. C.S. acknowledges financial support from the Alexander von Humboldt Stiftung. A.Z. acknowledges financial support from the Leverhulme Trust (grant number RPG-2020-038). Calculations were also performed on the Cambridge Service for Data Driven Discovery (CSD3) operated by the University of Cambridge Research Computing Service ([www.csd3.cam.ac.uk](http://www.csd3.cam.ac.uk)), provided by Dell EMC and Intel using Tier-2 funding from the Engineering and Physical Sciences Research Council (capital grant EP/P020259/1), and DiRAC funding from the Science and Technology Facilities Council ([www.dirac.ac.uk](http://www.dirac.ac.uk)). J.C. acknowledges funding from the National Natural Science Foundation of China under grant no. 11974024, and the Strategic Priority Research Program of Chinese Academy of Sciences under grant no. XDB33000000.

**Author contributions** V.K. and A.M. conceived the study. V.K. and C.S. developed the MLP. V.K., J.C. and C.J.P. implemented and performed structure search using the RSS scheme with the MLP. V.K. performed MLP simulations. J.C. performed first-principles simulations. A.Z. performed QMC calculations. V.K., C.S. and AM analysed the data, designed the figures and wrote the paper. All of the authors discussed the results and commented on the manuscript.

**Competing interests** The authors declare no competing interests.

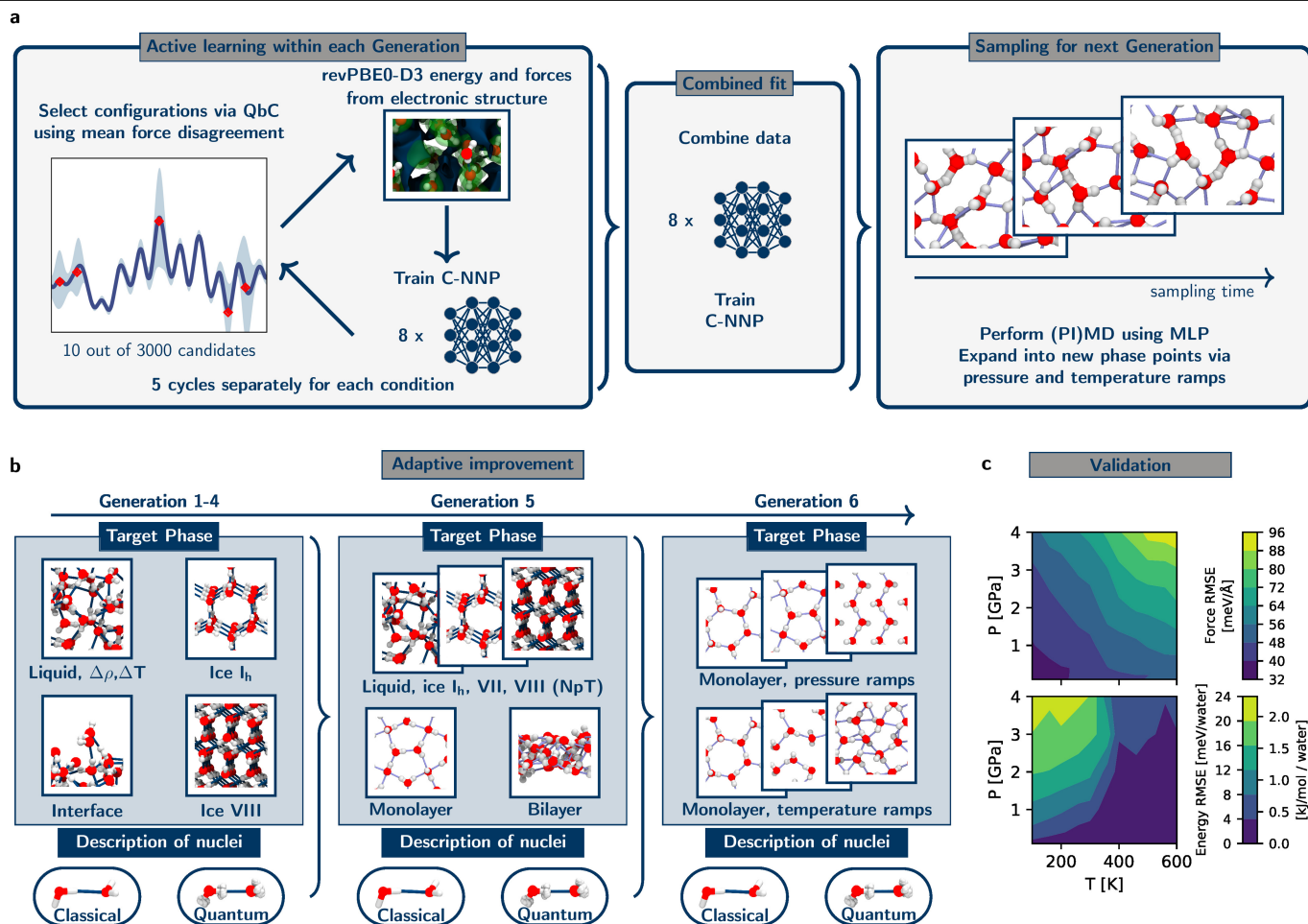
### Additional information

**Supplementary information** The online version contains supplementary material available at <https://doi.org/10.1038/s41586-022-05036-x>.

**Correspondence and requests for materials** should be addressed to Venkat Kapil, Christoph Schran or Angelos Michaelides.

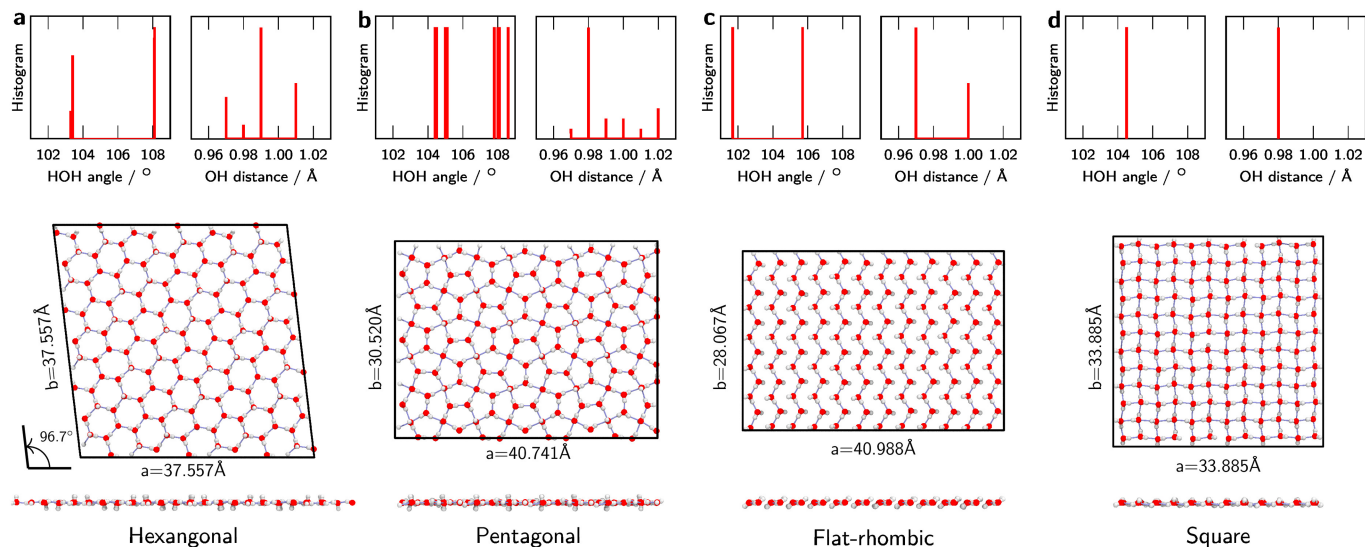
**Peer review information** *Nature* thanks Davide Donadio, Greg Kimmel and the other, anonymous, reviewer(s) for their contribution to the peer review of this work. Peer reviewer reports are available.

**Reprints and permissions information** is available at <http://www.nature.com/reprints>.



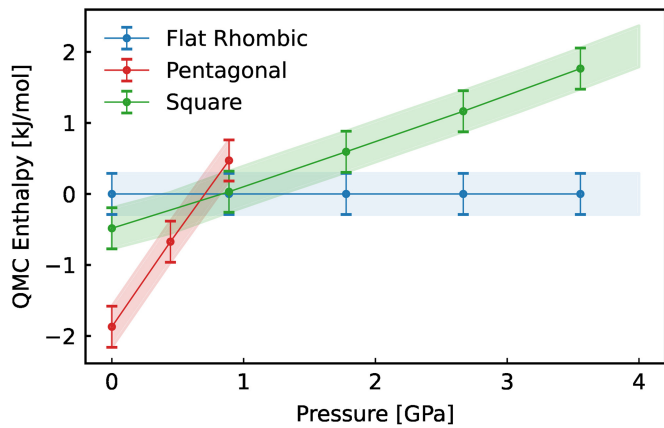
**Extended Data Fig. 1 | Active learning workflow of the machine learning potential across the full phase diagram.** (a) As depicted in the schematic, the main idea behind the machine learning potential is the combination of multiple neural network potentials (NNPs) in a “committee model”<sup>33</sup>, where the committee members are separately trained by random subsampling of the training set. Here we use a committee of 8 neural network potentials. The committee average provides more accurate predictions than the individual NNPs, and the committee disagreement, the standard deviation across the committee, is an estimate of the error of the model. To construct a training set of such a model in an automated and data-driven way, new configurations with the highest disagreement can be added to the training set. This approach is known as “query by committee” (QbC). (b) As shown in the schematic, the development of MLPs for various phase points is performed across different “generations”, such that in each generation new thermodynamic state points are targeted to yield an MLP which is used to sample new candidate structures for the next generation. We used the bulk water potential from ref.<sup>33</sup>, trained on 814 configurations of liquid water, different ice phases, and the water-vacuum

interface, all including nuclear quantum effects. In the next generation we added 521 new structures of classical and path integral *NPT* simulations of monolayer, bilayer water, bulk water and hexagonal ice (100–400 K and 0–1 GPa), ice VII and ice VIII (100–400 K and 0.8–10 GPa), and two sets of monolayer and bilayer ice structures from ref.<sup>18</sup>. In the final generation we added 207 structures from classical and path integral *NPT* temperature and pressure ramps of monolayer water (100–400 K and 0–5 GPa). We obtain an energy and force root mean square error (RMSE) for the training set of 2.4 meV per H<sub>2</sub>O (or 0.2 kJ mol<sup>-1</sup>) and 75.4 meV Å<sup>-1</sup>, respectively. (c) Force (top) and energy (bottom) root mean square error (RMSE) of an independent validation set covering the explored phase diagram of mono-layer confined water. The largest force RMSE for this validation set is with 100 meV Å<sup>-1</sup>, suggesting that the model remains accurate and robust across a wide range of temperature and pressure. The new model also keeps its excellent performance for the original condensed phase conditions, as noted by a predicted density of 0.93 kg l<sup>-1</sup> and a melting temperature of 270 ± 5 K at ambient pressure, in excellent agreement with the reference functional<sup>31</sup>.

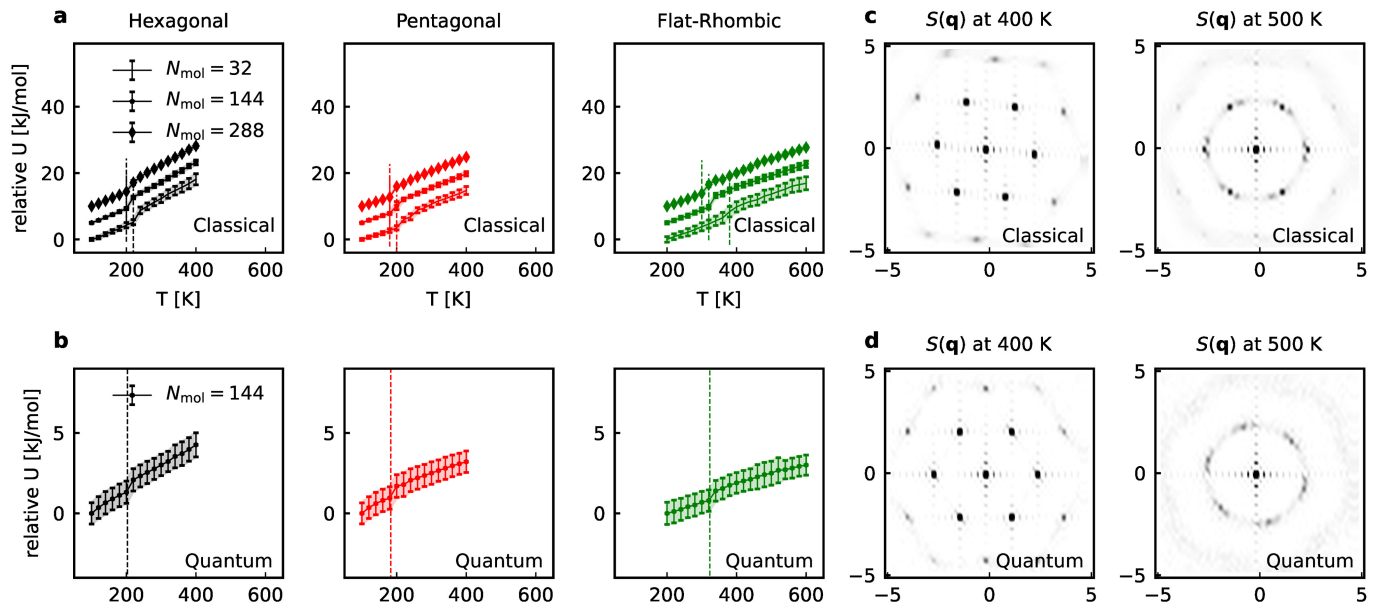


**Extended Data Fig. 2 | Monolayer ice phases.** (a) Top and side view of the monolayer hexagonal phase. (b) Top and side view of the monolayer pentagonal phase. (c) Top and side view of the monolayer flat-rhombic phase. (d) Top and

side view of the monolayer square phase. Lattice constants are labelled along cell vectors. Insets show histograms of O–H distances and H–O–H angles for the optimized structures following the approach from ref. <sup>18</sup>.

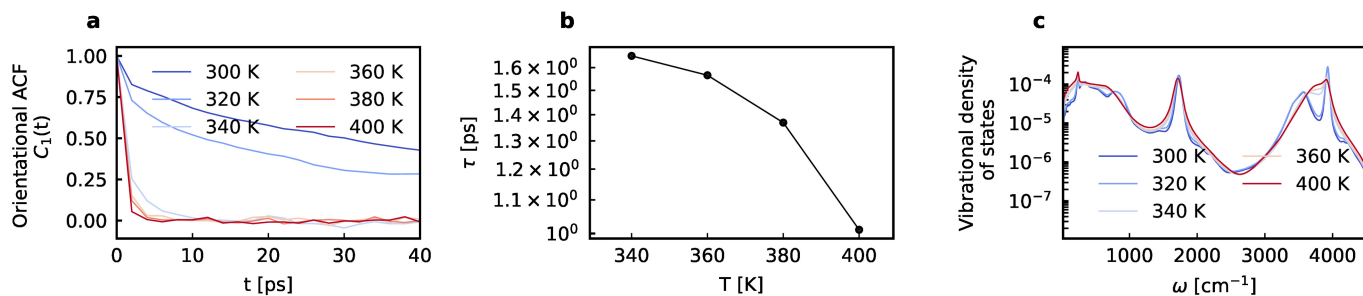


**Extended Data Fig. 3 | Zero temperature (classical) phase diagram at quantum Monte Carlo level.** The pressure dependence of the lattice enthalpies of the pentagonal (red) and square (pink) phases relative to the flat-rhombic (green) phase calculated at QMC level. Error bars indicate stochastic QMC error.



**Extended Data Fig. 4 | Sensitivity analysis of coexistence lines with respect to finite size and quantum nuclear effects. (a)** The temperature dependence of the potential energy for simulations initialized with monolayer hexagonal, pentagonal and flat-rhombic ice phases at 0 pressure, 0.5 GPa and 1.0 GPa respectively. The number of water molecules in the simulation cell are indicated in the legend, with larger (smaller) marker sizes corresponding to larger (smaller) system sizes. The potential energy of the curves have been translated vertically to make it easier to discern the temperature of melting (indicated by a vertical dashed line) for different systems sizes. Shaded regions indicate statistical uncertainty. **(b)** The temperature dependence of the

potential energy for simulations initialized with monolayer hexagonal, pentagonal and flat-rhombic ice phases at 0 pressure, 0.5 GPa and 1.0 GPa respectively, with nuclear quantum effects. Shaded regions indicate statistical uncertainty and the melting temperature is indicated by a vertical dashed line. **(c)** The structure factor of monolayer confined water in the hexatic phase (400 K) and at the transition between the hexatic and the liquid phase (500 K), without nuclear quantum effects. **(d)** The structure factor of monolayer confined water in the hexatic phase (400 K) and at the transition between the hexatic and the liquid phase (500 K), with nuclear quantum effects.



**Extended Data Fig. 5 | Rotational dynamics of monolayer hexatic water.**

**(a)** 1st order orientational autocorrelation function of the hexatic phase at 1 GPa from 340 to 400 K calculated as  $C_1(t) = \langle P_1[\nu(0) \cdot \nu(t)] \rangle$  where,  $\nu(t)$  is the orientation of the O–H bond at time  $t$ , and  $P_1$  is the Legendre polynomial of degree one. **(b)** Temperature dependence of the 1st order orientational relaxation time, computed as the time integral of  $C_1(t)$ , for the O–H molecular axis of the hexatic phase at 1 GPa. The relaxation time at 340 K is around seven times smaller than that of room temperature liquid water, indicating facile

rotation of water molecules in the hexatic-like phase. **(c)** The vibrational density of states across the flat-rhombic (up to 320 K) to the hexatic-like phase transition (beyond 340 K) as calculated by the Fourier transform of the velocity autocorrelation function. The flat-rhombic phase is characterized by two distinct vibrational bands for hydrogen bonded and dangling O–H bonds, and clear features for the librational modes. On the other hand, the rotations in the hexatic-like phase merge the two stretching bands into a doublet, and smear out the fine structure of the librational band.

Extended Data Table 1 | Relative lattice energies of variable-cell optimized monolayer ice structures

Polymorph	Lattice enthalpy [kJ/mol]					
	At 0.0 GPa			At 2.0 GPa		
	DFT	NNP	QMC	DFT	NNP	QMC
Hexagonal	0.0	0.0	0.0	-	-	-
Pentagonal	0.5	0.2	0.4	4.8	4.5	3.3
Flat-Rhombic	2.3	1.3	2.2	0.0	0.0	0.0
Square	3.0	3.1	1.5	3.0	1.8	1.0

Relative lattice enthalpies of different polymorphs of monolayer confined water calculated using revPBE0-D3, the corresponding MLP developed in this work, and quantum Monte Carlo (QMC) – the reference level of theory used to select the DFT functional. QMC values have been taken from ref. <sup>21</sup> for all structures, except for the newly found flat-rhombic phase which was computed as part of this study using exactly the same computational settings as in ref. <sup>21</sup>. The dashed entries (-) suggest that the structure is not stable at the indicated pressure.

## Extended Data Table 2 | Sensitivity analysis of coexistence lines with respect to the parameters of the confinement potential

Potential	Changes in transition pressure [GPa]					
	H-P			P-R		
	20 K	60 K	120 K	20 K	100 K	200 K
0 Leg	0.000	0.000	0.000	0.008	0.006	0.001
1 Leg	0.003	0.001	0.010	0.022	0.165	0.030
2 Leg	0.001	0.001	0.005	0.116	0.087	0.016

Change in the transition pressure between the hexagonal (H), pentagonal (P) and the flat-rhombic (R) phases, arising from changing the parameters of the Morse potential used in this work to those of Morse potentials fitted to the QMC interaction energies of a (i) 0-leg, (ii) 1-leg, and (iii) 2-leg water molecule, taken from ref. <sup>43</sup>. The confining potential used in this work is a Morse potential fitted to interaction energies of all the three types of water configurations. The changes in the transition pressures were calculated using thermodynamic perturbation theory. We note that these changes within statistical errors of the coexistence lines of the predicted phase diagram and suggest that a confinement that explicitly incorporate C-H interactions should lead to the same qualitative phase diagram.

## Extended Data Table 3 | Sensitivity analysis of coexistence lines with respect to the confinement width

Change in width [Å]	Changes in transition pressure [GPa]					
	H-P			P-R		
	20 K	60 K	120 K	20 K	100 K	200 K
0.1	0.000	0.000	0.003	0.045	0.034	0.011
0.2	0.001	0.001	0.006	0.090	0.067	0.021
0.5	0.003	0.002	0.015	0.226	0.168	0.053

Change in the transition pressure between the hexagonal (H), pentagonal (P) and the flat-rhombic (R) phases at given temperatures due to small change in the confinement width calculated using thermodynamic perturbation theory. These suggest that the predicted phase diagram is robust with respect to small changes in the confinement width.